X-622-69-285

PREPRINT

NASA TM X- 63619

A COMPARISON BETWEEN OBSERVED WINDS AND CLOUD MOTIONS DERIVED FROM NIMBUS II HRIR MEASUREMENTS

WILLIAM E. SHENK
EARL R. KREINS

JULY 1969

GSFC — GODDARD SPACE FLIGHT CENTER —
GREENBELT, MARYLAND

X-622-69-285

A COMPARISON BETWEEN OBSERVED WINDS AND CLOUD MOTIONS DERIVED FROM NIMBUS II HRIR MEASUREMENTS

William E. Shenk

and

Earl R. Kreins, Major USAF

July 1969

GODDARD SPACE FLIGHT CENTER

Greenbelt, Maryland

A COMPARISON BETWEEN OBSERVED WINDS AND CLOUD MOTIONS DERIVED FROM NIMBUS II HRIR MEASUREMENTS

William E. Shenk

and

Earl R. Kreins, Major, USAF

ABSTRACT

Cloud motions over oceanic areas were obtained from HRIR measurements contained within the overlapped region of two adjacent Nimbus II orbits. These 108-minute averaged motions were compared with instantaneous wind vectors interpolated from constant pressure charts. Corrections for uncertainties in the attitude of the satellite were made by superimposing coastlines that were within the fields of view for both orbits. Cloud mass centroids were determined to estimate the position for each cloud. Cloud top altitudes were obtained from the Nimbus II HRIR data and the isotherms on the constant pressure charts. Generally, the direction and speed of the cloud motions were within 20° and 15 knots of the observed wind direction and speed.

CONTENTS

A COMPARISON BETWEEN OBSERVED WINDS AND CLOUD MOTIONS DERIVED FROM NIMBUS II HRIR MEASUREMENTS

William E. Shenk

and

Earl R. Kreins, Major, USAF*

BACKGROUND

One of the primary objectives of the Global Atmospheric Research Program (GARP) is the determination of winds at several levels in the atmosphere and with 400 km horizontal spacing. Present and planned efforts to accomplish this task are by tracking constant pressure balloons and by measuring the speed and direction of cloud movements as detected by visible and infrared sensing devices on board satellites placed in geosynchronous orbit. To date, only visible sensors have been placed in synchronous orbit on board the Applications Technology Satellites (ATS), and the reported research results indicate that judiciously selected small clouds can serve as atmospheric tracers. The most widely employed technique to obtain cloud motions from the ATS data is based on the ability to identify a cloud element on a series of successive photographs taken at intervals of approximately 20 minutes and then measure the cloud displacement from the first photograph to the last. Since the visible data provide no clear indication of cloud height, the clouds have been assigned to statistically determined preferred

*Air Weather Service member temporarily attached to the Goddard Space Flight Center. Present affiliation: Joint Meteorological Satellite Program Office, Headquarters USAF, Washington, D.C.

pressure levels (one each for low and high clouds) or to the pressure level where the conventionally observed wind most closely approximates the cloud motion. Generally, the results from these techniques have been the determination of wind direction to within 20° and speeds to within 10 knots. Infrared sensors placed in geosynchronous orbit should provide more definitive information on cloud top heights.

Most of these comparisons between cloud motions and wind observations have been performed within 50° of great circle arc of the subsatellite point. Figure 1 illustrates the geometric relations along a great circle passing through the subsatellite point between local zenith angle δ, nadir angle Φ and great circle arc θ. As the distance from the subsatellite point increases, a cloud is viewed more obliquely. As a result, greater difficulty is encountered in accurately identifying and locating a cloud element. Thus, it would be expected that cloud motions determined where δ is large would be less accurate and compared less favorably with the observed winds than where δ is small.

Figures 2 and 3 show the portions of the Northern Hemisphere that would be covered by three and four equally spaced equatorial geosynchronous satellites, respectively, within three different limits of δ. Coverage over North America was purposely given low priority since this is one region where conventional meteorological data are adequate. With the system of three geosynchronous satellites, complete coverage at the equator is accomplished with $\delta = 70°$. If a four satellite system is employed, then complete coverage is assured to 30°N

within $\delta = 60°$. Let it be assumed that at $\delta = 60°$ the capability to determine winds from the geosynchronous satellite has dropped to the point when alternate methods would receive strong consideration. Even with the four geosynchronous satellite coverage, cloud motion information would not provide wind estimates over large areas of the North Atlantic and North Pacific oceans. In the Southern Hemisphere, with its larger percentage of ocean surface to land surface, the oceanic data gaps would be more extensive.

The concept of wind measurement from satellites was mentioned long before the launch of TIROS I (Widger, 1957). Greaves (1965) tried to implement the concept by recognizing that there is considerable overlap in the data from adjacent orbits at high latitudes for satellites with highly inclined orbits. Using TIROS IX video data, the cloud displacements from one orbit to the next were computed after corrections were applied for parallax and for the attitude differences between orbits by matching recognizable landmarks in each orbit. These computed motion vectors were then compared with 500 mb geostrophic winds. The computed directions were generally within 30° of the observed direction except for three vectors where the average error was 140°. These three vectors were estimated from what were judged to be cirrus clouds well above the 500 mb surface. Generally, the computed speeds were substantially less than the 500 mb geostrophic winds with which they were compared. This effort suffered from the inability of the video data to locate the cloud at a specific level.

The above discussion illustrates several key points. First, the visible data from the equatorial geosynchronous satellite may not be able to provide accurate

wind measurements at large local zenith angles and will provide only daytime information. Second, when the preferred levels technique is used, wind information is assigned to only two levels. Also, although the technique of obtaining winds from the video data in the overlapped region of the two adjacent orbits from a near polar orbiting satellite showed some promise, there was still an obvious need for better cloud top height estimates. Therefore, the ideal sensor to provide winds at high latitudes would be a polar orbiting satellite with sufficient resolution to see some cloud detail and give information on cloud top height. The High Resolution Infrared Radiometer (HRIR) on board the Nimbus I, Nimbus II and Nimbus III satellites comes closest to this ideal. For this study, the Nimbus II HRIR was chosen. Besides the search for a useful method for obtaining winds at high latitudes, this study can also examine the general question of the feasibility of obtaining winds from radiometric measurements.

NIMBUS II SATELLITE

The Nimbus II satellite was launched into a near-circular retrograde sun-synchronous polar orbit with an inclination of 100.3°, apogee and perigee heights of 1179 km and 1095 km, respectively, and a nodal period of 108.17 minutes. A complete description of the spacecraft system is given in the Nimbus II Users' Guide (1966).

HIGH RESOLUTION INFRARED RADIOMETER DATA

The Nimbus II High Resolution Infrared Radiometer (HRIR) sensed upwelling radiation in the 3.5-4.1 atmospheric "window" with a resolution which was 8.6 by

9.7 kilometers at the subsatellite point from an orbital attitude of 1100 km. In this wavelength region, thermal emission and reflected solar radiation contribute about equally to the observed radiance during the daytime. Therefore, only at night is the detection of pure thermal radiation possible. Moonlight reflection from the earth is negligible. Thus, at night, reasonable meteorological interpretations of terrestrial radiation patterns can be made. The detected radiances are converted to equivalent blackbody temperatures. These derived temperatures are used to determine surface temperatures, under clear sky conditions, and cloud top heights where the clouds are assumed to be opaque and completely fill the view of the radiometer.

The radiometer scanned perpendicular to the orbital track of the satellite. Space radiance levels are viewed along part of the scan while the radiometer is not pointing towards the earth. In the course of data processing and after converting the radiances to effective blackbody temperatures, the computer averages the effective blackbody temperatures over the space portion of the scan. All effective blackbody temperatures that fall below this averaged value during the earth scan are given a value of 190 K. Since the average effective blackbody temperature associated with the space scans during the lifetime was 225 ± 5 K except for a short period following launch, any averaging of these temperatures with other effective blackbody temperatures above the space threshold might result in fictiously low temperatures. Omitting the 190's would give a bias toward effective blackbody temperatures that are too warm. Thus, temperatures that

are near the threshold and where data from more than one scan spot were averaged must be cautiously interpreted.

The infrared data currently are available in two forms. One is a photographic image produced from the analog records. The other, a grid print map, is a computer display of the data rectified for various scales and map projections. More complete descriptions regarding these two types of data dispiay can be found in the Nimbus II Users' Guide (1966) and in other publications such as Warnecke, et al., (1968).

The measurements from the HRIR contain both periodic and random noise components. Spectral analysis revealed a strong 200 Hz noise component caused by interference from the spacecraft clock. This can be largely removed by numerical filtering, and a computer subroutine written by McMillin (1969) is part of the standard mapping program.

Williamson (1969) has investigated the random noise of the HRIR measurements. He calculated the noise equivalent temperature difference, NEΔT, for the HRIR at several temperatures. For a radiometric measurement, NEΔT is defined as the change in target temperature which would produce a change in measured response equal to the r.m.s. noise at the output of the instrument. Figure 4 is reproduced from Williamson's paper and shows NEΔT for a single digitized sample as a function of target temperature. It is apparent that for temperatures colder than 240 K the NEΔT become large, even for data treated by McMillin's filter. In order to improve the temperature resolution at a given

grid point on a grid print map, the number of digitized samples, N, must be increased since the data error at any grid point is the error of any given sample divided by $\sqrt{N}$. Some data resolution must be sacrificed if improved temperature resolution is desired.

The sun shade on the HRIR was not sufficiently large to prevent some additional solar energy from affecting the measurements. These effects, as shown by the streaks in the pictorial presentation (Figure 5) between approximately 55 N and 70 N, and in an analyzed grid print map (Figure 6) for a small portion of Figure 5, are most noticeable when the sun was near the satellite horizon. No cloud motion calculations were performed within these regions.

PROCEDURE

The first step was to select two adjacent orbits with HRIR coverage at high latitudes so that there was considerable overlap in the two data fields. A Mercator map projection was used with a scale of 1:2 million. Thus, at the equator, this scale gives a distance of 15 nautical miles between grid points, while at a latitude of 60° the distance is approximately 8 nautical miles due to the geometry of the projection. Except at nadir angles very close to 50° at high latitudes, there was at least one measurement present at each grid point. Close to the subsatellite point, the reported effective blackbody temperature at each grid point was derived from the averaged data from several scan spots.

From orbit to orbit there is a random error in locating the radiation data on the grid print maps. This error results from uncertainties in the attitude of

the satellite. These location errors can be as much as 30 nautical miles. This attitude error alone could result in sizeable differences between apparent cloud motions and the corresponding observed winds. A method to reduce this error is to demand that a distinquishable land feature be detectable in both orbits. Then the coastlines, lakes, etc. can be matched and allowances made for the differences in attitude between orbits.

Another location error is due to inaccurate determination of the relative location of successive scans (Sabatini and Sissala, 1969). This is caused by the errors in locating both horizons during the course of a scan. At the subsatellite point, this error is about 3 nautical miles and is somewhat greater nearer the horizons. Since this error is much smaller than the attitude error and since there is no simple technique of correcting for it over large areas, no correction was applied.

Following the determination of the distance that one map had to be shifted to correct for attitude errors, individual cloud elements were selected that could be identified on both maps. Clouds that were in or very near surface frontal zones were avoided because of the expected sizeable influence of strong vertical motions near the front. Frontal zone clouds have the tendency to drift with the front and be poorly related to the winds moving through the front. Also, no cloud motion calculations were performed where the cloud top temperature was less than 240 K due to the nearness to the space threshold and the increase in random noise at cold temperatures. The centroid of each cloud mass was

computed and the movement of the centroid from the earlier to later map was called the computed cloud motion.

The effects of parallax must be considered when an object that is closer to the viewing platform than the background is located on its background and is viewed from two different points in space. Figure 7 presents an exaggerated view. Since the clouds were geographically placed by referencing the earth's surface and the clouds are above the surface, the apparent zonal component of motion is more than the real zonal motion for the retrograde Nimbus II orbit. As the satellite moves through a full orbit, the earth rotates beneath it at a rate of 15° of longitude per hour. Therefore, at the equator, a point has moved about 3010 km eastward during one Nimbus II orbital period. Thus, for a stationary cloud top at 6 km above the earth's surface with the satellite at an altitude of 1100 km, there is an apparent 19 km easterly motion of the cloud. Thus, considering the orbital period of the satellite, the apparent rate of movement would be 6 knots. At 60° N, this apparent rate of movement diminishes to 3 knots due to the smaller easterly shift of a point during an orbital period. Since most of the cloud motions computed were in the latitude range from 40° N - 60° N, no parallax correction was applied unless a cloud top was placed above 500 mb. Then, a 5 knot westward component was added.

There are several assumptions that are necessary in order to place a cloud top at a pressure level and to geographically place the centroid. It must be assumed that in the region where there is an apparent cloud that the cloud top

surface completely fills the field of view of the radiometer and it must be further assumed that the cloud is opaque. The failure of either assumption means that the apparent cloud top level is lower than the true level. To minimize the effect of these assumptions, the centroid was computed using the coldest region of the apparent cloud. A third assumption is that the cloud moves with the wind at the cloud top; in other words, the cloud is wafer thin. Serebreny et al., (1969), comparing cloud motions computed from ATS pictures and observed winds has indicated that this assumption is reasonable.

Another consideration in the vertical placement of the cloud tops is the temperature corrections that could be applied to the HRIR data due to the interference of atmospheric constituents. The principal interfering atmospheric constituents are carbon dioxide and water vapor. At the earth's surface over the range of nadir angles from 0° to 50°, corrections for these two constituents average about 3 K (Warnecke, McMillin and Allison, 1969). Naturally, above the surface where the masses of carbon dioxide and water vapor are less, the corrections would be smaller. Since 3 K corresponds to an average altitude error of about 0.3 km and most corrections would be smaller than 3 K, no corrections were applied.

Instead of assigning the coldest individual value at a grid point within the area used to compute the centroid, a spatial average of several points was taken as representative of the effective cloud top temperature. This further reduces the effect of random noise and gives ample weight to a sizable amount of the

cloud top surface. The pressure level of the cloud top was determined by matching the effective cloud top temperature to the same temperature determined by interpolating that temperature from constant pressure charts at the standard pressure levels. Then, the observed wind at the determined pressure level was interpolated from these conventional charts.

Figure 8 shows the two data fields used to locate and identify a cloud element as well as the comparison between the computed cloud motion and the observed wind.

DATA SELECTION

In order to minimize the random errors in data location introduced by satellite attitude variations, a noticeable thermal difference between water and land was necessary because of the coastline matching that is essential to the procedure. This nighttime thermal contrast between the land and the warmer water is greatest in the fall season during the six month period of available Nimbus II data. Therefore, all the cases selected were during the late summer and the fall seasons. Table 1 lists the orbital pairs, the midpoint time between the orbits, and the geographical features used to adjust for relative attitude errors.

Synoptic situations were selected where most of the computed cloud motions were over water. Since the orbital period is 108 minutes, it becomes essential to minimize possible distortions in the cloud over this interval. Rough terrain influences changes in cloud shape, cloud height, and apparent cloud motions due to preferred regions of cloud development and dissipation. Not only do these

influences lead to erroneous cloud motions but they also increase the likelihood that a cloud will not be properly identified in the second orbit as the same cloud that was viewed in the first orbit.

Over and east of Asia, the Daily Weather Map series supplied by the Japan Meteorological Agency (1966) was the conventional meteorological data source used to extract the wind measurements and the temperature information necessary to fix the pressure level of the cloud top. This series contained charts at the mandatory levels from surface to 500 mb. Above 500 mb, National Meteorological Center (NMC) charts supplied the same information. Over North America, all interpolations were made from NMC mandatory level charts.

For the Asian synoptic cases, no observed wind interpolations were performed between the 1200 GMT constant pressure charts (closest time to the satellite passes) and the 0000 GMT constant pressure charts for the next day, except for one case. In this case, a rapidly moving short wave trough was propagating through the area causing large wind fluctions in a short time. Therefore, some adjustment was made to the 1200 GMT observed winds using the observed wind field displayed on the following set of 0000 GMT charts. The midpoint times between each orbital pair were generally around 1500 GMT (See Table 1).

Space and time interpolation was performed for the North American cases since the midpoint time for the adjacent orbits was about 0600 GMT.

SAMPLE CASE

A complete discussion of one of the seven cases will be presented followed by tabulation of pertinent data for the other six. The sample case to be discussed occurred November 11, 1966, with the midpoint time of 1530 GMT between the two adjacent orbits (data orbits 2400 and 2401). Figure 9 shows the amount of overlap in the HRIR data for the two orbits. Extensive portions of the China coastline and the Korean peninsula were clearly discernible in both orbits. A sharp 10 K temperature difference between land and water marked the position of the China coast and a lesser difference was observed to indicate the Korean coastline. These temperature gradients were then superimposed and the amount of attitude error between orbits determined.

Table 2 lists the appropriate information of each comparison made between the seven computed cloud motions and observed winds. Figure 10 shows a schematic comparison of the computed vectors and the observed winds plus the determined cloud top levels. No adjustment in the observed winds was made between the conventional map time (1200 GMT) and the midpoint time for the two orbits. Five of the seven computed cloud motions were from the simple translation of a cloud element but the other two were attempts to use other techniques.

The first of these was a very prominent cloud edge. Figure 11 shows two views of this cloud edge for the two orbits. Instead of a centroid computation, the position of the edge was indicated at the midpoint of the edge and in the strongest thermal gradient. Selection of the appropriate temperature to vertically

locate the cloud top was more subjective. This cloud edge appears to be the leading edge of a middle and high cloud shield moving off the Asian coast. Since cirriform clouds form at least part of the shield, it seems plausible that the radiometer is viewing a cloud that is not completely opaque. Therefore, the observed HRIR gradient from east to west is probably due to an emissivity gradient rather than a substantial change in the height of the cloud or the amount of cloud filling the field of view of the radiometer. Thus, more weight was given in the cloud height determination to the effective temperatures well behind the cloud edge. Table 2 indicates that 245 K was the average effective temperature selected. This estimate could easily be off by ±5 K. The interpolated cloud top level was 450 mb and the computed cloud motion was 275 degrees at 65 knots with a 5 knot westerly component being subtracted due to parallax. The interpolated observed wind at 450 mb was 280 degrees at 70 knots.

Another technique was the use of a hole in the clouds. This hole, shown in Figure 12 for the two orbits, was in the same general cloud mass that produced the prominent cloud edge to the northeast. The movement of the hole is controlled by the movement of the surrounding clouds. Therefore, the pressure "level" of the hole should be estimated from the surrounding cloud tops. A pressure level of 425 mb was assigned to the average effective temperature of 245 K and the cloud direction and interpolated wind direction agreed to within 15 degrees while the cloud and observed wind speeds were the same (60 knots).

HIGHLIGHTS OF THE OTHER CASES

Of the remaining six cases, four were near the Asian Coast and the other two over North America. All of the computed cloud motions in the Asian cases were over water and all of the cloud vectors computed over North America were over land. Table 3 gives a complete list of the computed cloud motions for the six cases. In addition to the simple translation of cloud elements the centroid of an ensemble of small clouds was computed and the displacement of the ensemble measured. The comparison between the cloud motion and the concurrent wind was within 10 degrees and 10 knots.

The greatest disparities between computed cloud motion direction and observed wind direction were noted in five computations which occurred over land between 850 mb and the surface. Four of the five cloud motions were computed for clouds over the Laurentian shield of eastern Canada and the fifth over the hilly terrain of northeastern Wisconsin. It is possible that there could be enough land influence on the clouds to cause the observed directional differences of 30 - 40 degrees. These five vectors are marked with an asterisk in Table 3 and will be specially considered in the statistical analysis in the next section.

STATISTICAL ANALYSIS

Figure 13 shows the frequency distribution of the cloud top heights. The distribution appears to be trimodal, reflecting some tendency for clouds to be either low, middle, or high.

Figure 14 is a cumulative frequency diagram for the entire data sample which shows the numerical change in the effective blackbody temperature from the first to the second view of each cloud. There was only a 3 K change in the cloud top temperature in 108 minutes for over 60% of the clouds used as tracers. The majority of this amount of temperature fluctuation could be caused simply by viewing the cloud at different nadir angles from one orbit to the next. Over 85% of the clouds had an effective blackbody temperature change of ≤ 6 K. Of the five clouds with orbit to orbit effective blackbody temperature changes of >7 K, two of these were a cloud edge pair and the hole in the clouds. These results suggest that little convective activity was connected with the tracer clouds. This is not surprising since the clouds were sensed at high latitudes where minimal convective activity would be expected. The small temperature changes also indicate that non-convective cloud top temperatures are conservative with time.

Figures 15 and 16 respectively show plots of computed cloud direction versus observed wind direction and computed cloud speed versus observed wind speed. The 45° angle line in both figures represents a perfect correlation. The cloud motions where substantial topographical influence is suspected are labelled with an X. Since a high percentage of winds have a westerly component, there is a natural bunching of data points between 220° and 320° in the direction scatter diagram. The scatter appears to be about equally divided on either side of the perfect correlation line. Thus, no consistent directional bias in the computed

cloud motions is present. In the speed scatter diagram, there appears to be a slight tendency for the computed speeds to be higher than the observed speeds. This effect may be due to cloud propagation. More likely, it reflects the inability of the radiometer to verify that the field of view is completely cloud filled and that the cloud top is not completely opaque. These latter effects mean that some of the contributed radiance to the total sensed radiance is emitted from within or below the cloud. The results of these effects are that the true cloud tops are probably higher than those indicated by the radiometer. The opacity effect is probably greatest where the clouds are close to the cirrus level. Kuhn and Weickmann (1969) have reported that emissivities associated with cirrus are substantially less than 1.0. Thus, since the wind speeds normally increase with height below the tropopause, the observed wind speeds would have more closely approximated the cloud speeds at some higher level.

Court (1958) and Durst (1954) have developed statistical relations to compute vector correlation coefficients. Court's total vector correlation coefficient, R_{wz} is more complete. Let

$$\sum_{k=1}^{n} W_k$$

and

$$\sum_{k=1}^{n} Z_k$$

be two samples of winds where $W = iU + jV$ and $Z = iX + jY$ are wind vectors separated in time, in space, or in both time and space. The simple linear correlation coefficients, r_{ux}, r_{vx}, r_{uy}, r_{vy} and r_{xy} are contained in the expression for R_{wz} where u, v, x and y are deviations from the means $\bar{U}$, $\bar{V}$, $\bar{X}$ and $\bar{Y}$. The sample variances of u and v are written as S_u^2 and S_v^2, respectively. The expression for R_{wz}^2 is given as

$$R_{wz}^2 = \frac{S_u^2 \left(r_{ux}^2 + r_{uy}^2 - 2r_{ux}\, r_{uy}\, r_{xy}\right) + S_v^2 \left(r_{vx}^2 + r_{vy}^2 - 2r_{vx}\, r_{vy}\, r_{xy}\right)}{\left(S_u^2 + S_v^2\right)\left(1 - r_{xy}^2\right)}$$

The Durst coefficient, r_{wz}^2, is defined by

$$r_{wz}^2 = \frac{(\Sigma ux + \Sigma vy)^2}{\left(\Sigma u^2 + \Sigma v^2\right)\left(\Sigma x^2 + \Sigma y^2\right)}$$

and the notation is the same that is used in the preceding paragraph. Court's relation involves multiple correlation of these variables while Durst's is like the simple correlation of two variables. Lamberth (1966) compared results of the two coefficients on the same data sample and found that the values of R_{wz} are r_{wz} were similar except when $R_{wz} < 0.30$. However, Lenhard (1967) discusses some earlier work by Lenhard et al., (1963) where $R_{wz} = 0.70$ and $r_{wz} = 0.40$. He cautioned against computing only r_{wz}.

Two computations of R_{wz} and r_{wz} were performed. One set of computations was with the full data sample (43 pairs) and the other excluded the five pairs where topography possibly influenced the clouds. The results for each sample were identical, $R_{wz} = 0.85$ and $r_{wz} = 0.84$. The fact that R_{wz} and r_{wz} were the

same for the two samples shows that even though there was a relatively large error in direction between the low-level cloud motions and observed winds over hilly terrain, the small speed errors compensated.

There is no rigorous way to estimate the confidence limits for Court's R_{wz}. However, Court* suggested that a Fisher z transformation should be useful in testing the significance of linear correlation coefficients. In application of this test, comparison is then made with the normalized standard deviation, σ_z, equal to $1/\sqrt{2N-10}$, where N represents the number of independent data pairs.

In the use of the z transformation, the null hypothesis is that the correlation between the two populations is zero. The probability that the observed correlation between the samples could be due to accidental sampling is determined. In this study, it is assumed that the distribution of sample correlation coefficients that could be computed by further studies is not normal. This is a conservative view. The transformation, z, is given by $z = 1/2\ [\ell n(1 + r) - \ell n(1 - r)]$ where, in this case $r = R_{wz}$. As often is the case in meteorology, estimating the number of degrees of freedom is not straightforward. One sample contained 43 pairs and the other 38. However, the number of degrees of freedom is undoubtedly smaller due to spatial dependence between sample pairs within a given synoptic situation and some intercorrelation between synoptic situations. The number of degrees of freedom as suggested by Court is 2N-10. A conservative hypothesis would be to assume that the seven synoptic situations are independent but that

*personal communication, 1969

there is perfect correlation between pairs within each situation. A more reasonable degrees of freedom estimate probably lies in between this extreme and the extreme of complete pair independence. It was assumed that within any synoptic case, exactly two pairs were independent of one another (rather than the average number of six pairs). Thus, the number of the degrees of freedom, 2N-10, is 18. The student's t test relation is expressed as $t = z/\sigma_z$ which equals 5.48. For 18 degrees of freedom this value of t indicates that the probability of the correlation coefficient originating from an uncorrelated population would be less than 0.1%.

CONCLUSIONS

The primary conclusion of this investigation is that by using Nimbus II HRIR data from two adjacent orbits, it is possible to obtain representative cloud motions that correlate reasonably well with the observed winds. A substantial contribution to this positive result was undoubtedly the radiometer capability to more clearly determine cloud top height than is possible with visible data. This capability, at least in part, compensated for the poorer spatial and time resolution than is currently available in computing cloud motions from the ATS satellite visible data. Since the overlap between adjacent orbits is most sig ificant at high latitudes, this technique might be most useful in the determination of winds over high latitude oceanic regions. It follows that it should be possible to derive wind data from other radiometric measurements where the resolution and noise characteristics are the same or better than the Nimbus II HRIR. This

is important since there are active programs to place radiometers in geosynchronous orbit with the wind measuring capability as the primary scientific objective. Results as good or better than the above should be anticipated from geosynchronous altitude in view of the shorter interval between successive views of a cloud element.

ACKNOWLEDGMENTS

We are indebted to Dr. Frank L. Martin for his suggestion of computing the vector correlation coefficients and to Mr. William R. Bandeen for his careful scrutiny of the manuscript. Also, we appreciated the stimulation of constant discourse with numerous other members of the Planetary Radiations Branch of the Laboratory for Atmospheric and Biological Sciences.

REFERENCES

Court, A., 1958: "Wind Correlation and Regression," Scientific Report No. 3, Cooperative Research Foundation, San Francisco 18, California, 16 pp.

Durst, C. S., 1954: "Variation of Wind with Time and Distance," Geophysical Memoirs, No. 93, Meteorological Office, Air Ministry, London, England.

Greaves, J. R., J. C. Barnes, W. P. Smith, and W. K. Widger, Jr., 1965: "Cloud Feature Persistence in Satellite Pictures and its Applicability to Wind Determination", ARACON Geophysics Co., Concord, Mass., Final Report, Cwb-10988, 42 p.

Japan Meteorological Agency, 1966, "Daily Weather Maps," Tokyo, Japan.

Kuhn, P. M., and H. K. Weickmann, 1969: "High Altitude Radiometric Measurements of Cirrus", Journal of Applied Meteorology, 8(1), pp. 147-154.

Lamberth, R. L., 1966: "On the Use of Count's Versus Durst's Techniques for Computing Vector Correlation Coefficients", Journal of Applied Meteorology, 5(5), pp. 736-737.

Lenhard, R. W., Jr., A. Court, and H. A. Salmela, 1963: "Variability Shown by Hourly Wind Soundings", Journal of Applied Meteorology, 2, pp. 94-104.

Lenhard, R. W., 1967: "Comment on 'On the Use of Court's Versus Dursts Techniques for Computing Vector Correlation Coefficients'", Journal of Applied Meteorology, 6(3), pp. 583.

McMillin, L. M., 1969: "A Procedure to Eliminate Periodic Noise Found in Nimbus II High Resolution Infrared Radiometer Measurements", Allied

Research Associates, Inc., Concord, Mass., Technical Report No. 9, Contract NAS5-10343, 16 p.

Nimbus Project, 1966: "Nimbus II Users' Guide," Goddard Space Flight Center, Greenbelt, Maryland, 229 p.

Sabatini, R. R., and J. E. Sissala, 1969: "Nimbus Earth Resources Observations", Allied Research Associates, Inc., Concord, Mass., Technical Report No. 7, Contract NAS5-10343, 67 p.

Serebreny, S. M., R. G. Hadfield, R. M. Trudeau, and E. J. Wiegman, 1969: "Comparison of Cloud Motion Vectors and Rawinsonde Data", Final Report, ESSA Contract E-193-68, Stanford Research Institute, Menlo Park, California, 30 p.

Warnecke, G., L. J. Allison, E. R. Kreins, and L. M. McMillin, 1968: "A Satellite View of Typhoon Marie 1966 Development", Goddard Space Flight Center, Greenbelt, Maryland, NASA TN D-4757, 94 p.

Warnecke, G., L. M. McMillin, and L. J. Allison, 1969: "Ocean Current and Sea Surface Temperature Observations from Meteorological Satellites", Goddard Space Flight Center, Greenbelt, Maryland, NASA TN D- , 47 p.

Widger, W. K., Jr. and C. N. Touart, 1957: "Utilization of Satellite Observations in Weather Analysis and Forecasting," Bulletin of the American Meteorological Society, 38(9), pp. 521-533.

Williamson, E. J., 1969: "The Accuracy of the High Resolution Infrared Radiometer on Nimbus II", Goddard Space Flight Center, Greenbelt, Maryland, NASA X-622-69-313.

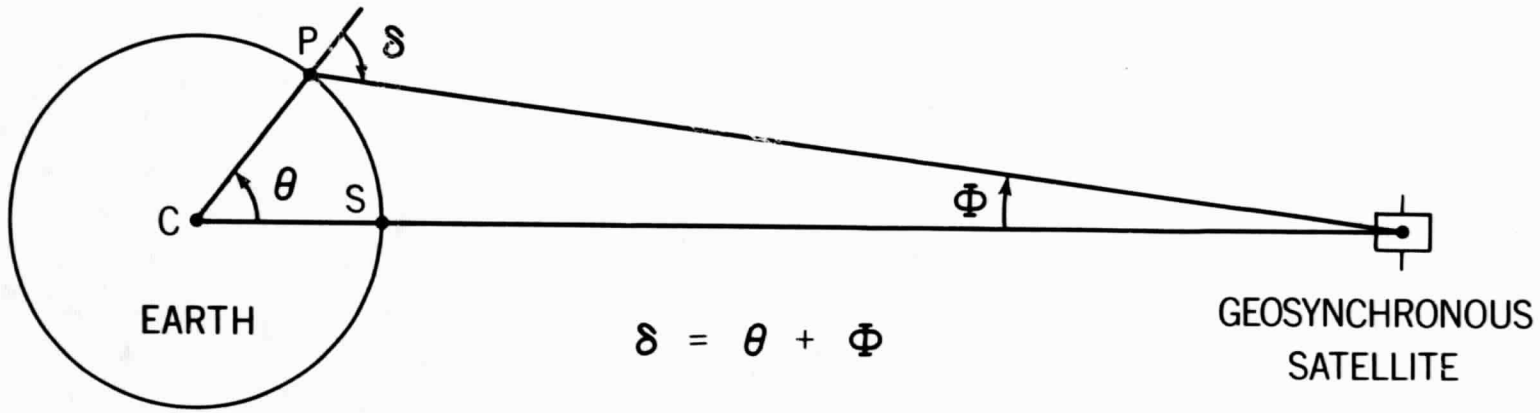

Figure 1. Geometric relations between nadir angle Φ, local zenith angle δ, and great circle arc θ for a satellite positioned in a geosynchronous orbit. Point P is an orbitrary point along the great circle, point S is the subsatellite point and point C is at the center of the earth.

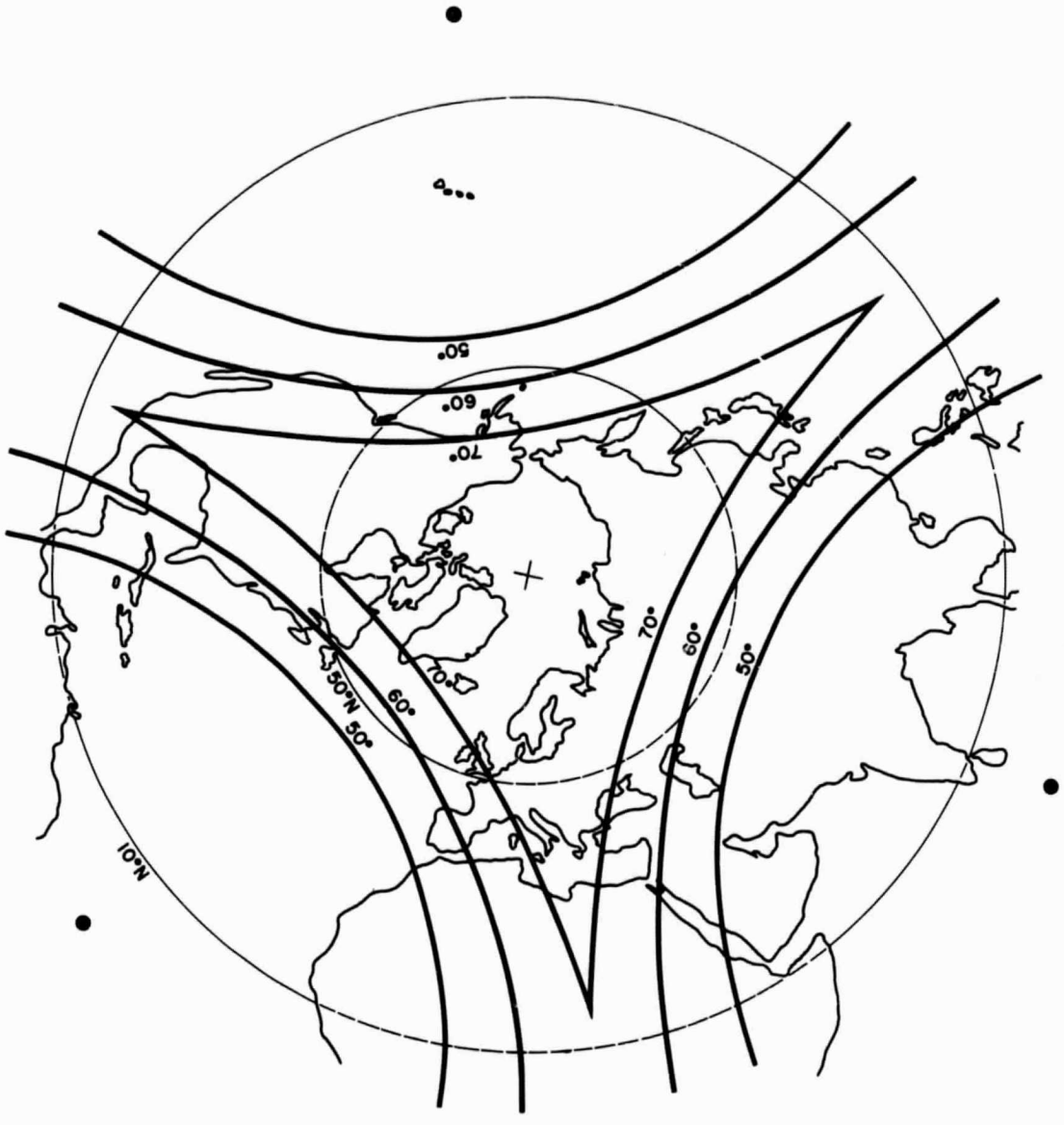

Figure 2. Northern Hemispheric coverage with a system of three equatorial geosynchronous satellites. Curved lines are lines of equal δ relative to each subsatellite point and the black dots indicate each subsatelliite point.

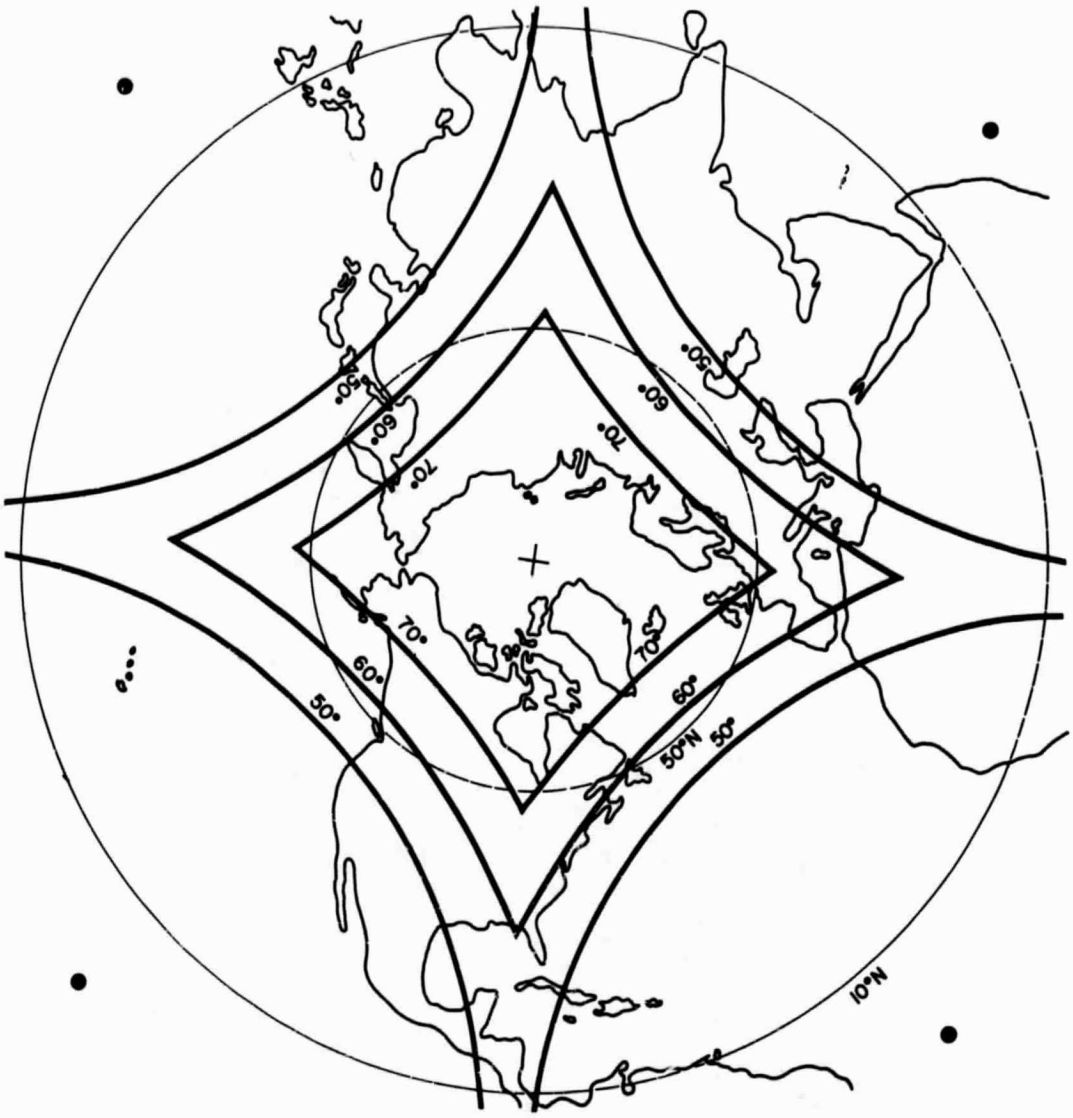

Figure 3. Northern Hemispheric coverage with a system of four equatorial geosynchronous satellites. The nomenclature is the same as Figure 2.

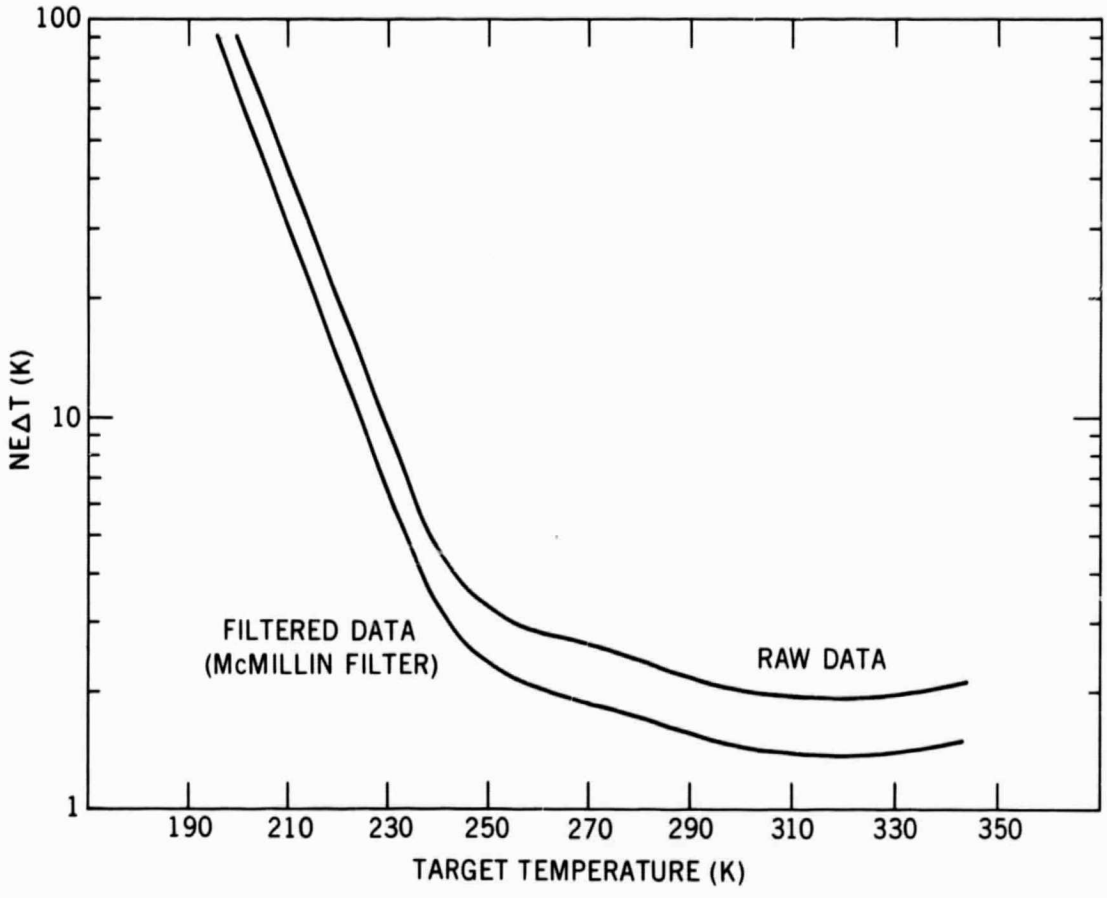

Figure 4. Noise equivalent temperature difference (NEΔT) for a single Nimbus II HRIR measurement.

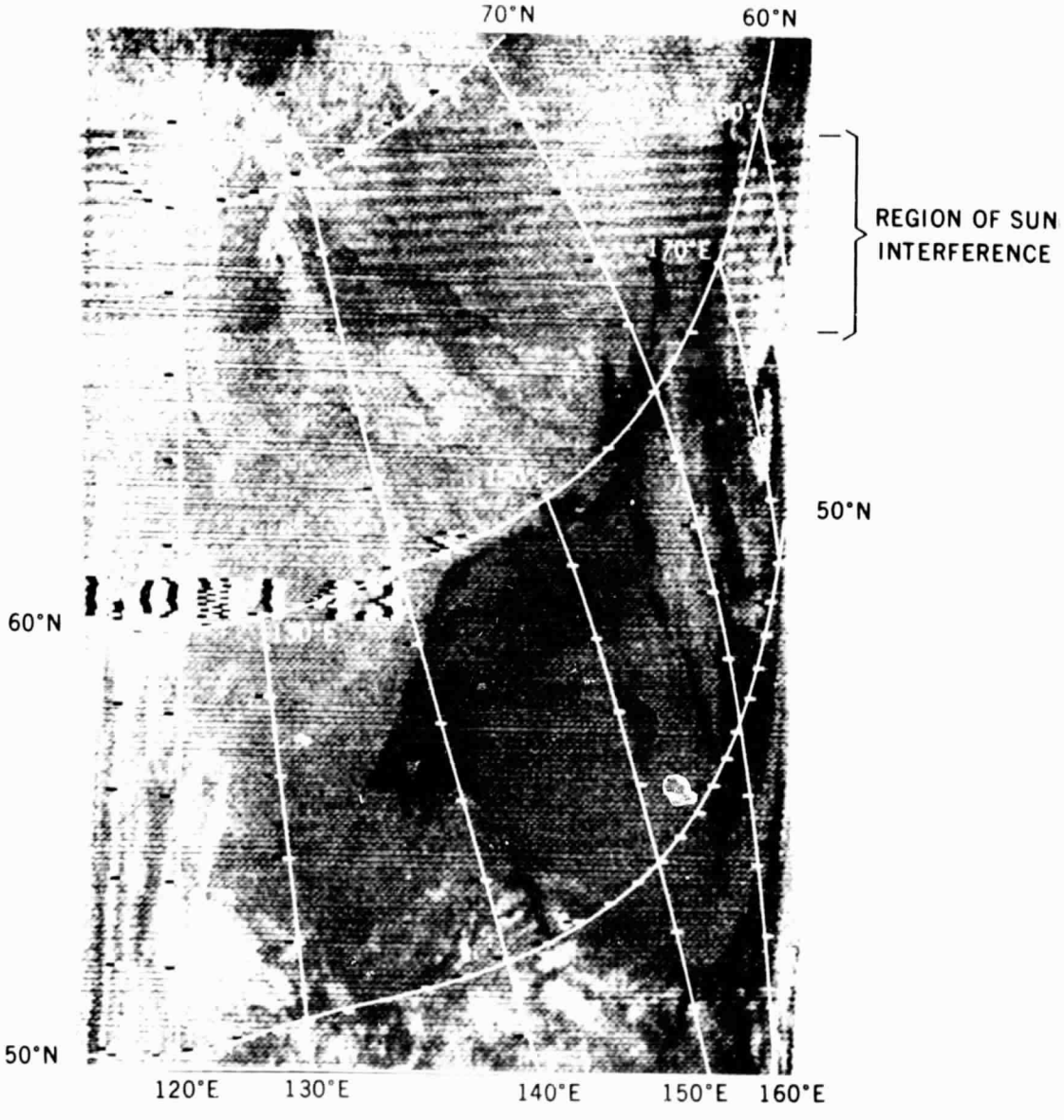

Figure 5. Example of sun interference in a pictorial HRIR presentation (Orbit 2041).

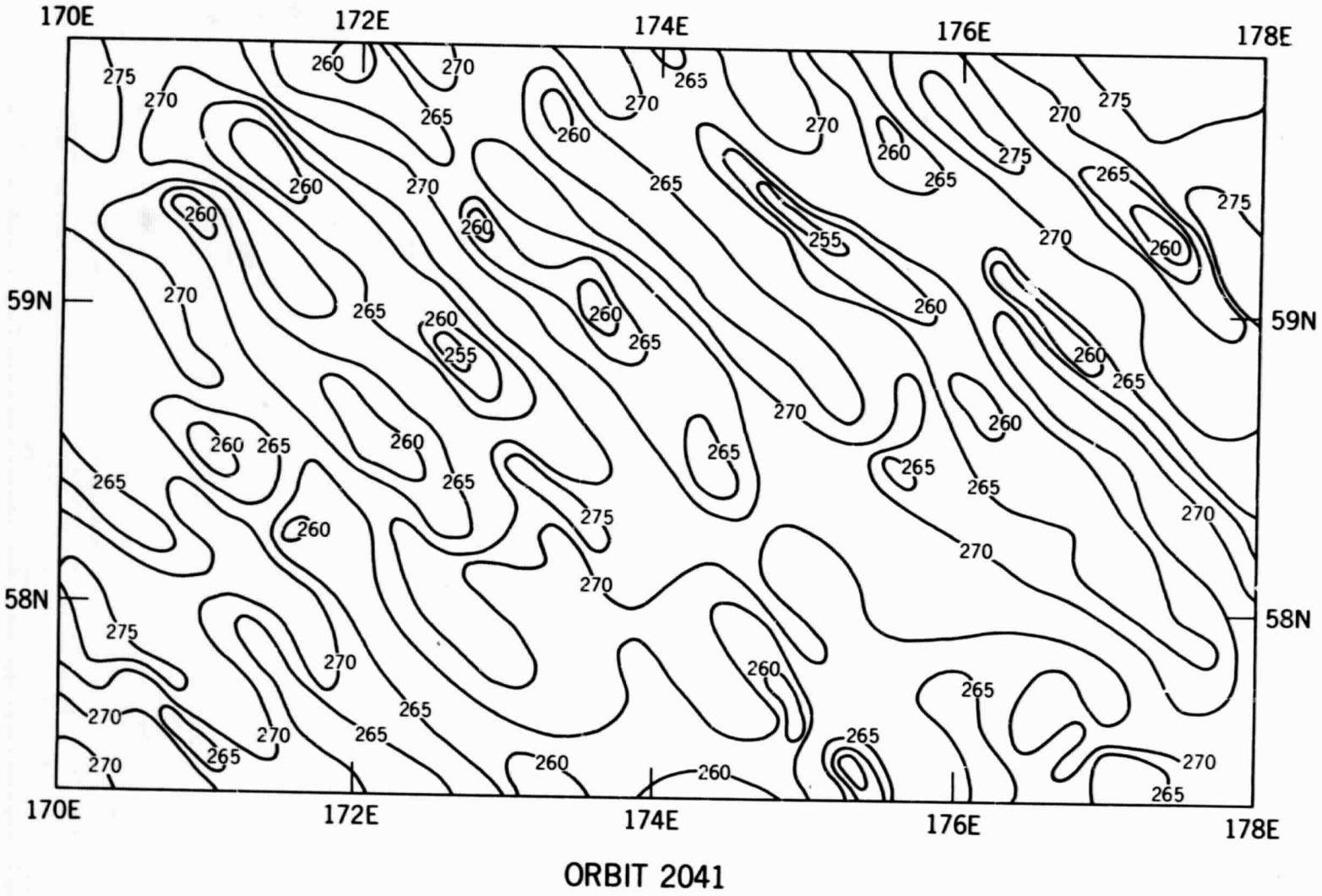

Figure 6. Example of the effect of sun interference on a HRIR grid print map display (Orbit 2041) as shown by the parallel lines of relatively warm and cold effective blackbody temperatures (°K).

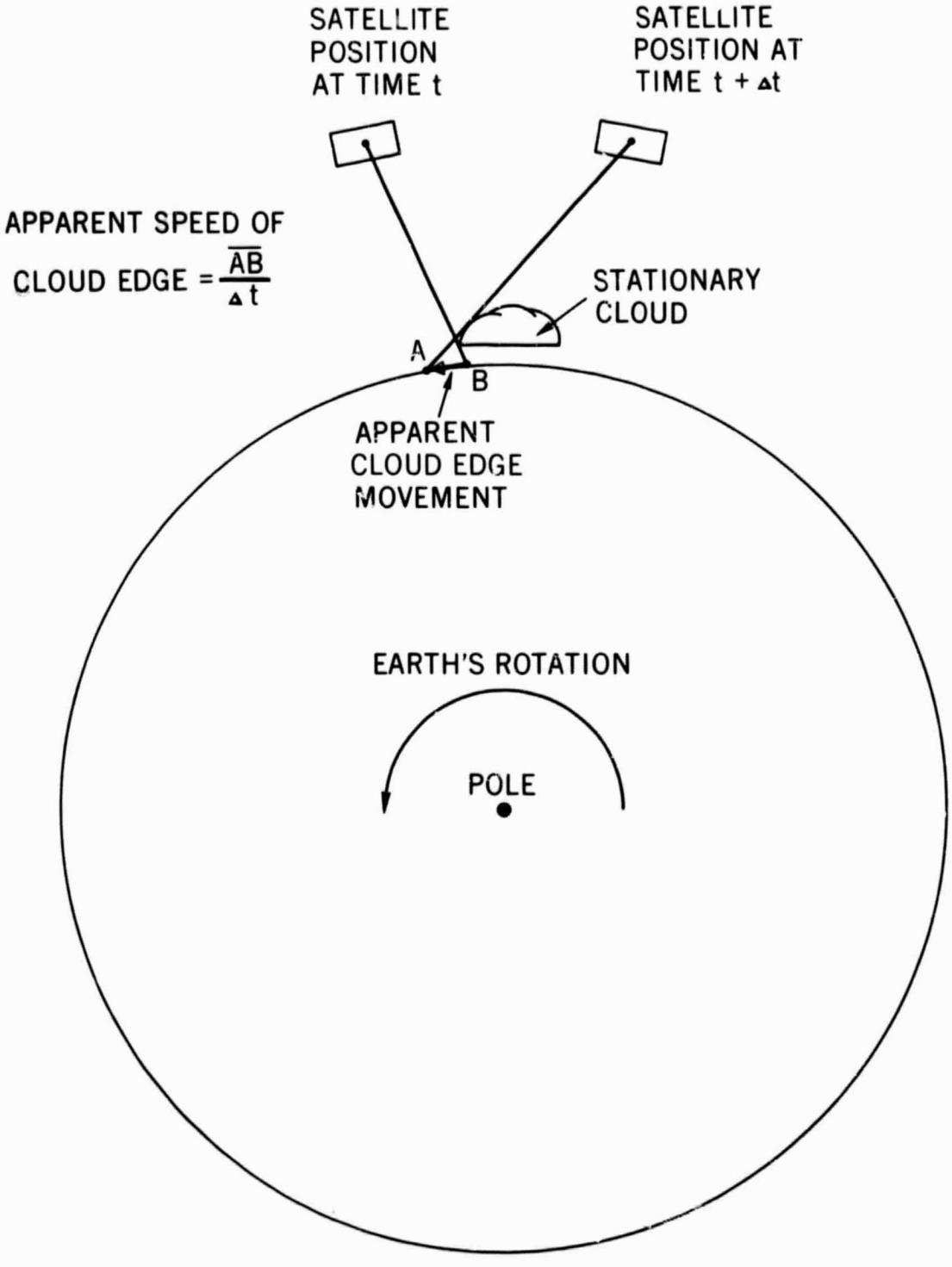

Figure 7. Apparent cloud edge motion due to parallax for a satellite with a retrograde orbit.

CLOUD MOTION COMPUTATION TECHNIQUE

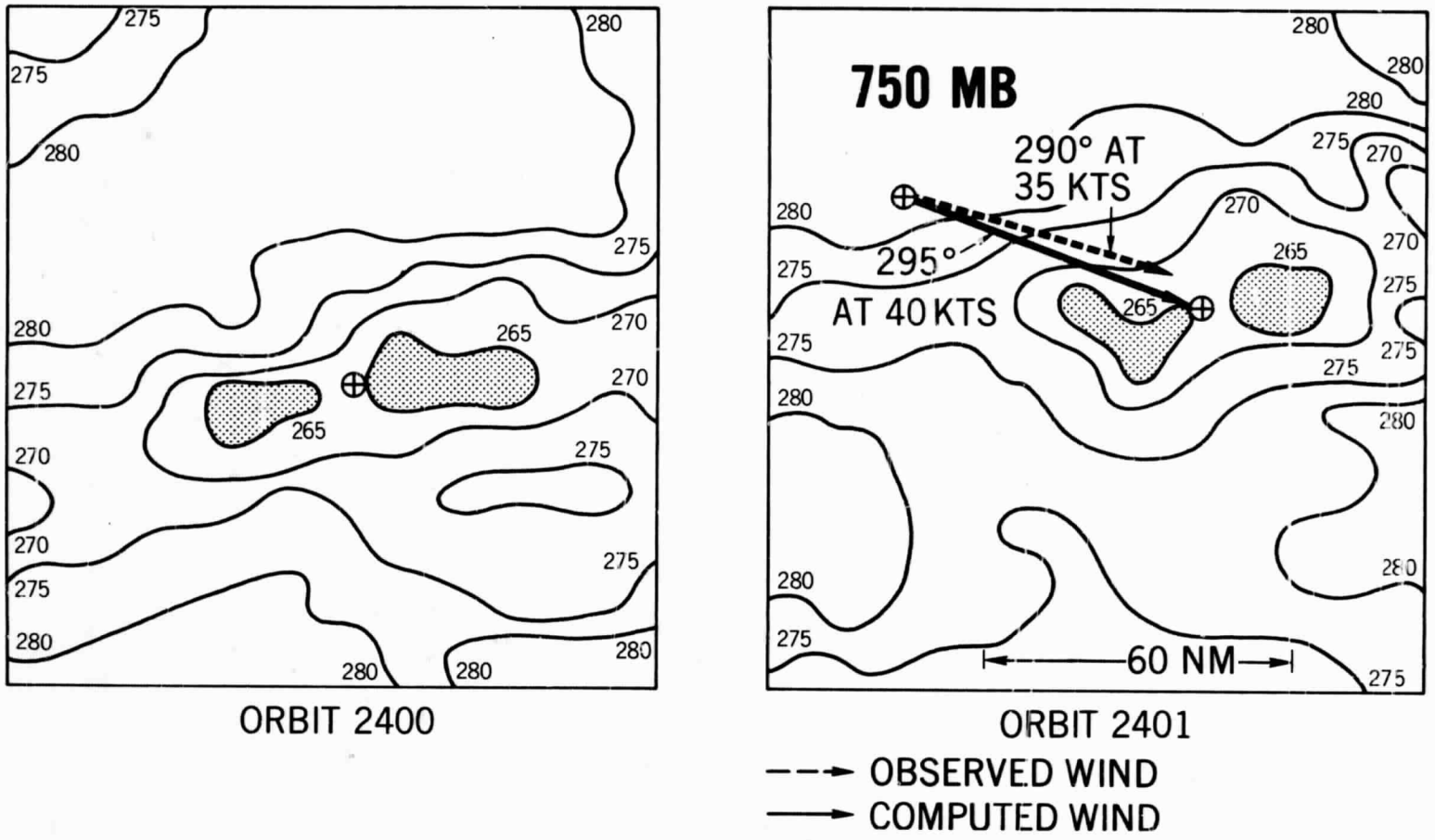

Figure 8. An example of a cloud pair that was used to obtain cloud motion and the comparison with the observed wind.

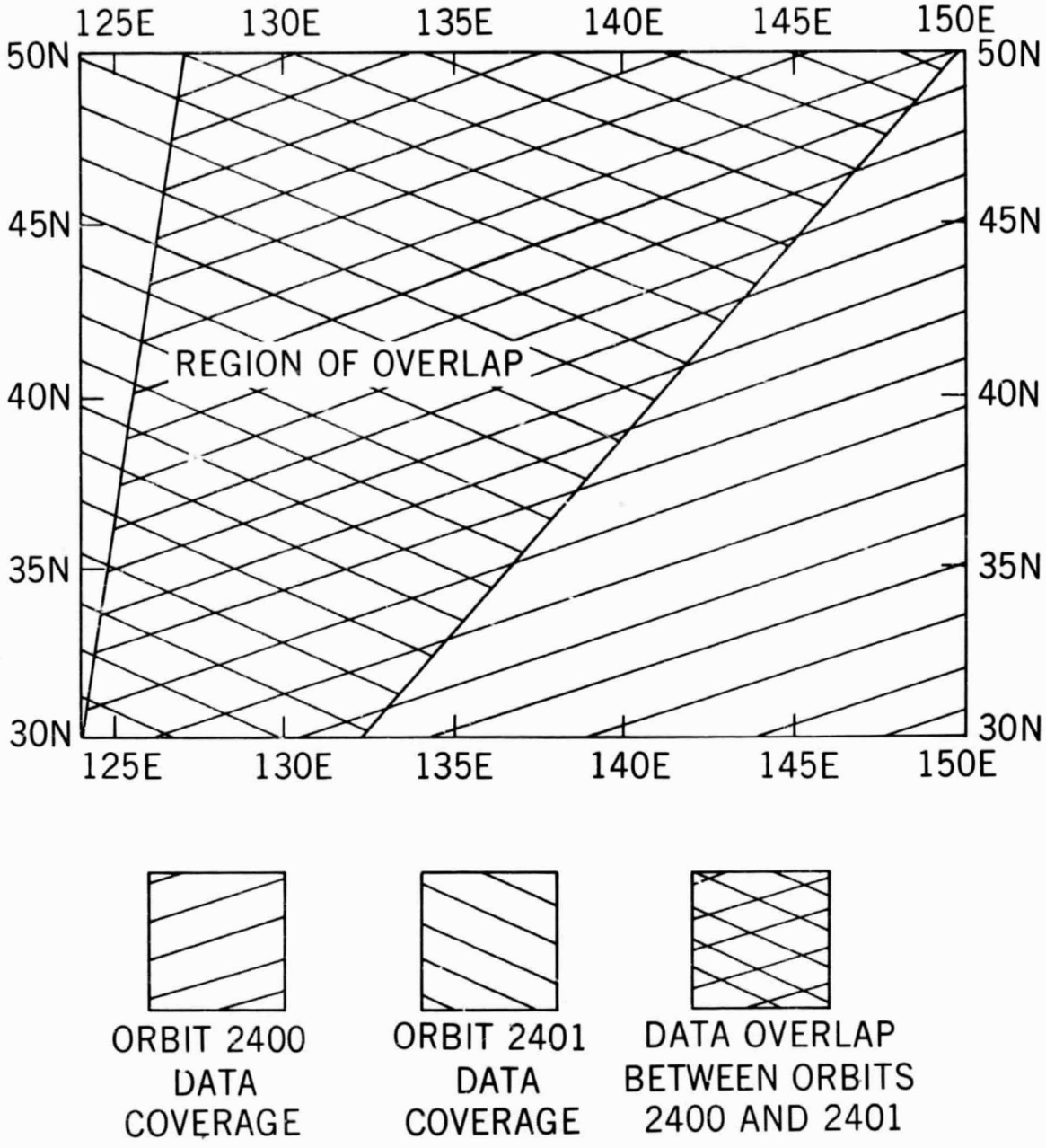

Figure 9. The amount of overlap in data coverage in the HRIR data fields from two adjacent orbits (2400 and 2401) with a nadir angle limit of 50°. Isotherms are in °K.

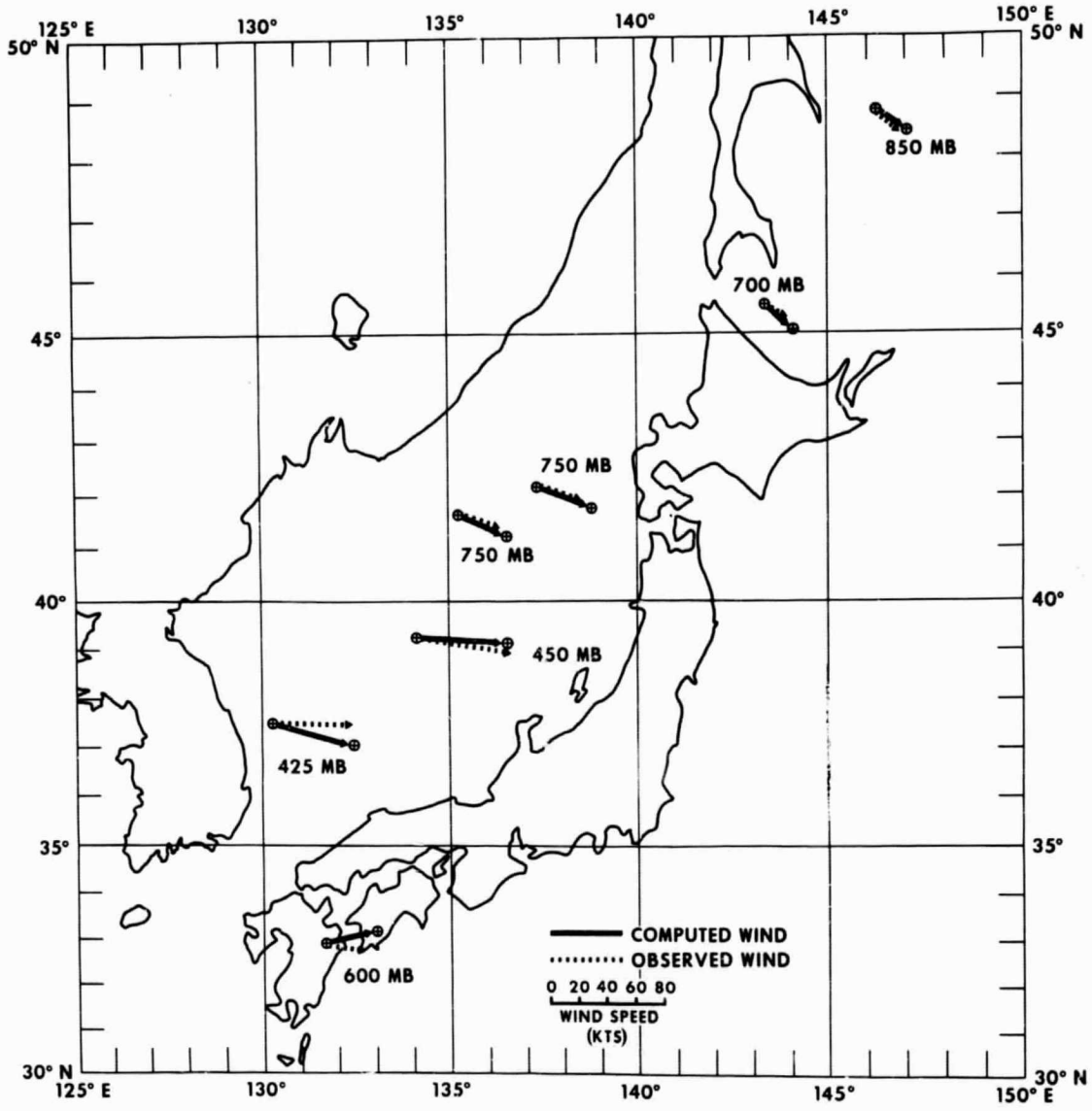

Figure 10. Schematic presentation of the seven cloud motions and observed winds for the case of November 11, 1966. The cloud top heights are shown in mb.

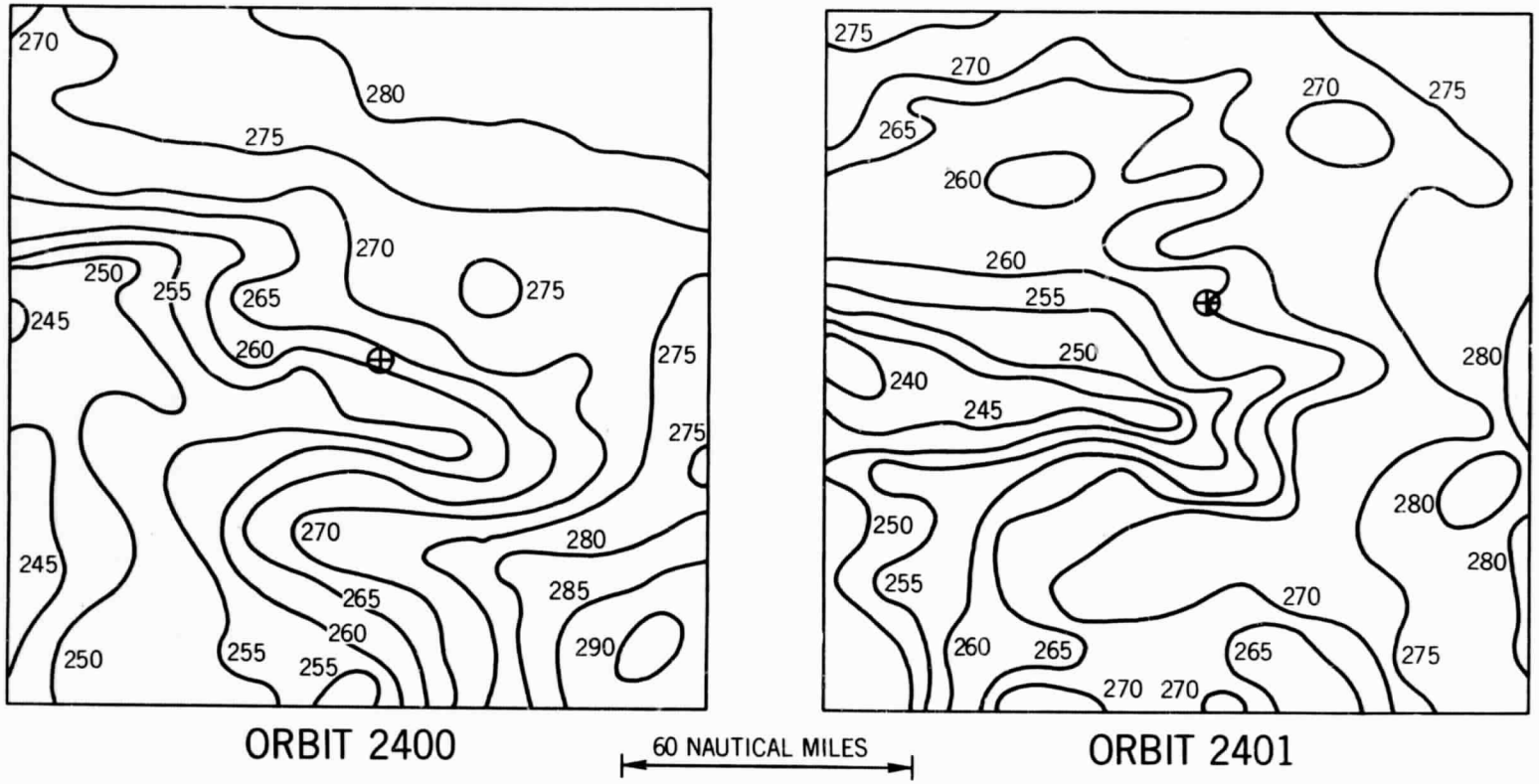

Figure 11. Prominent cloud edge as shown in orbits 2401 and 2402. Isotherms are in °K.

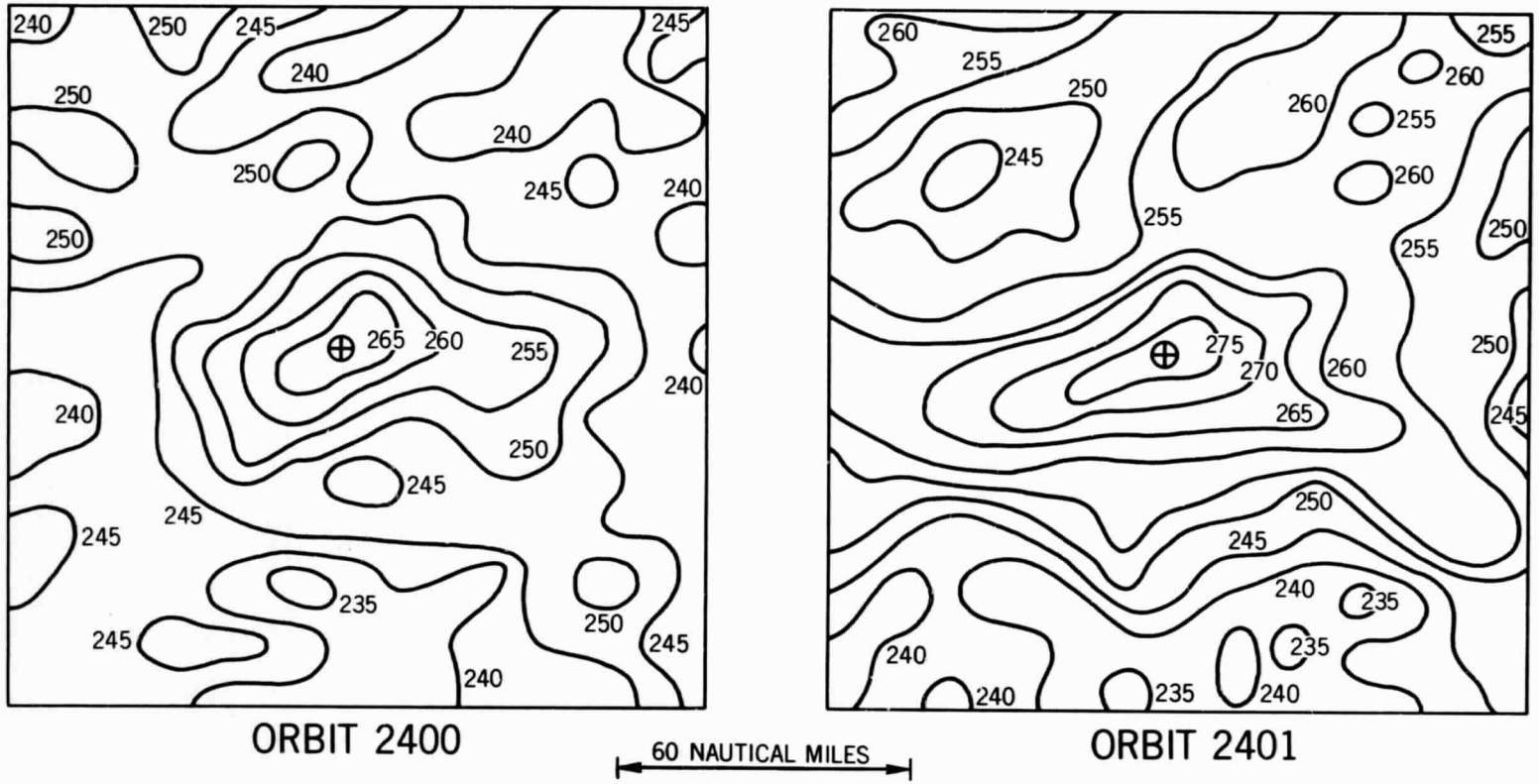

Figure 12. Well defined hole in an extensive cloud sheet (Orbits 2400 and 2401). Isotherms are in °K.

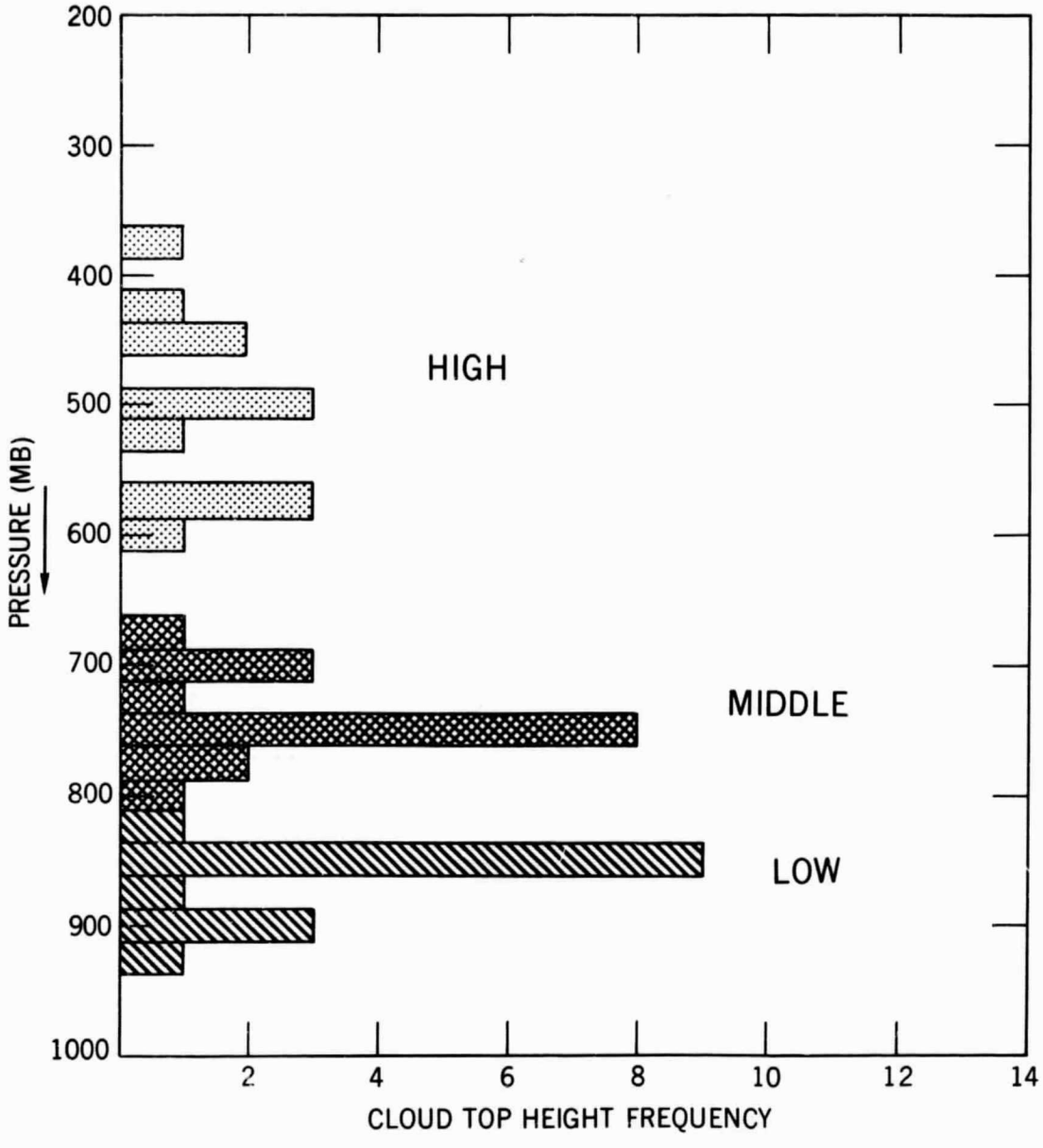

Figure 13. Frequency distribution of the cloud top heights. Class intervals of 25 mb.

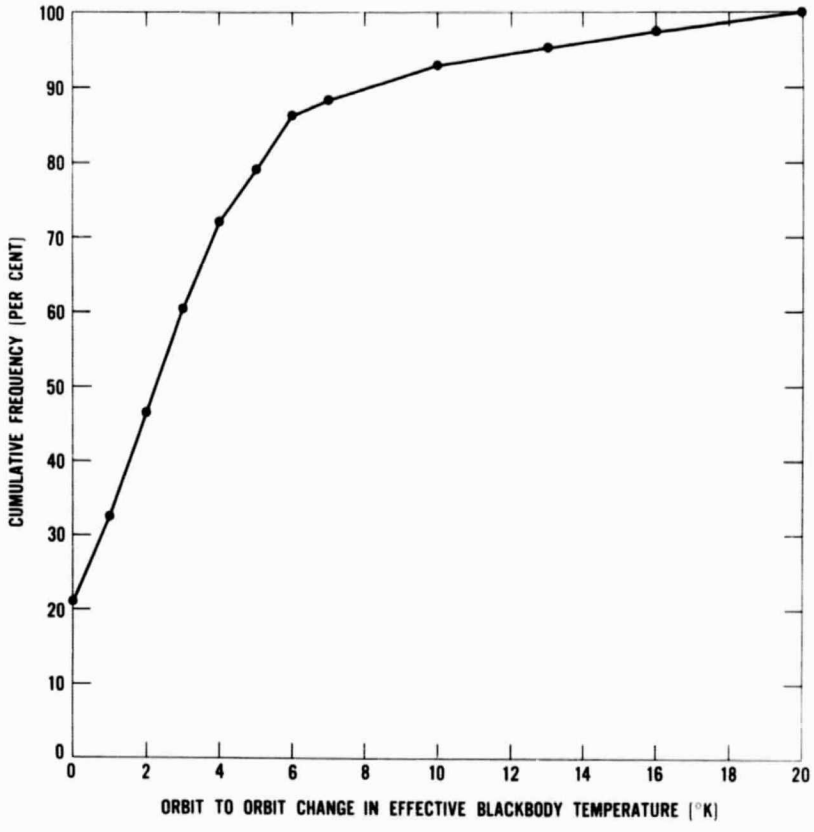

Figure 14. Cumulative frequency diagram of the orbit to orbit change in the effective blackbody temperatures of the cloud tops.

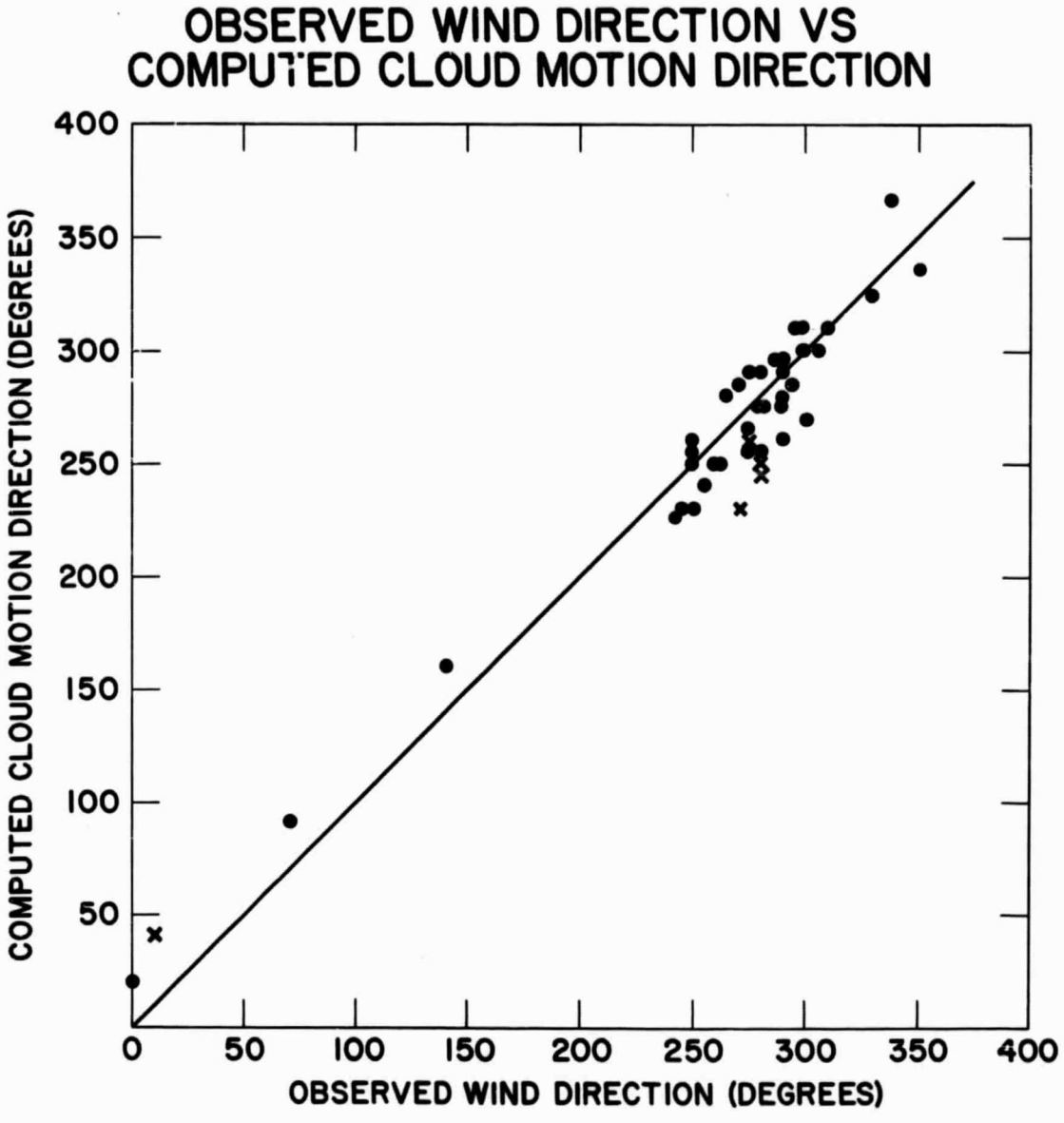

Figure 15. Scatter diagram of computed cloud motion diagram versus observed wind direction.

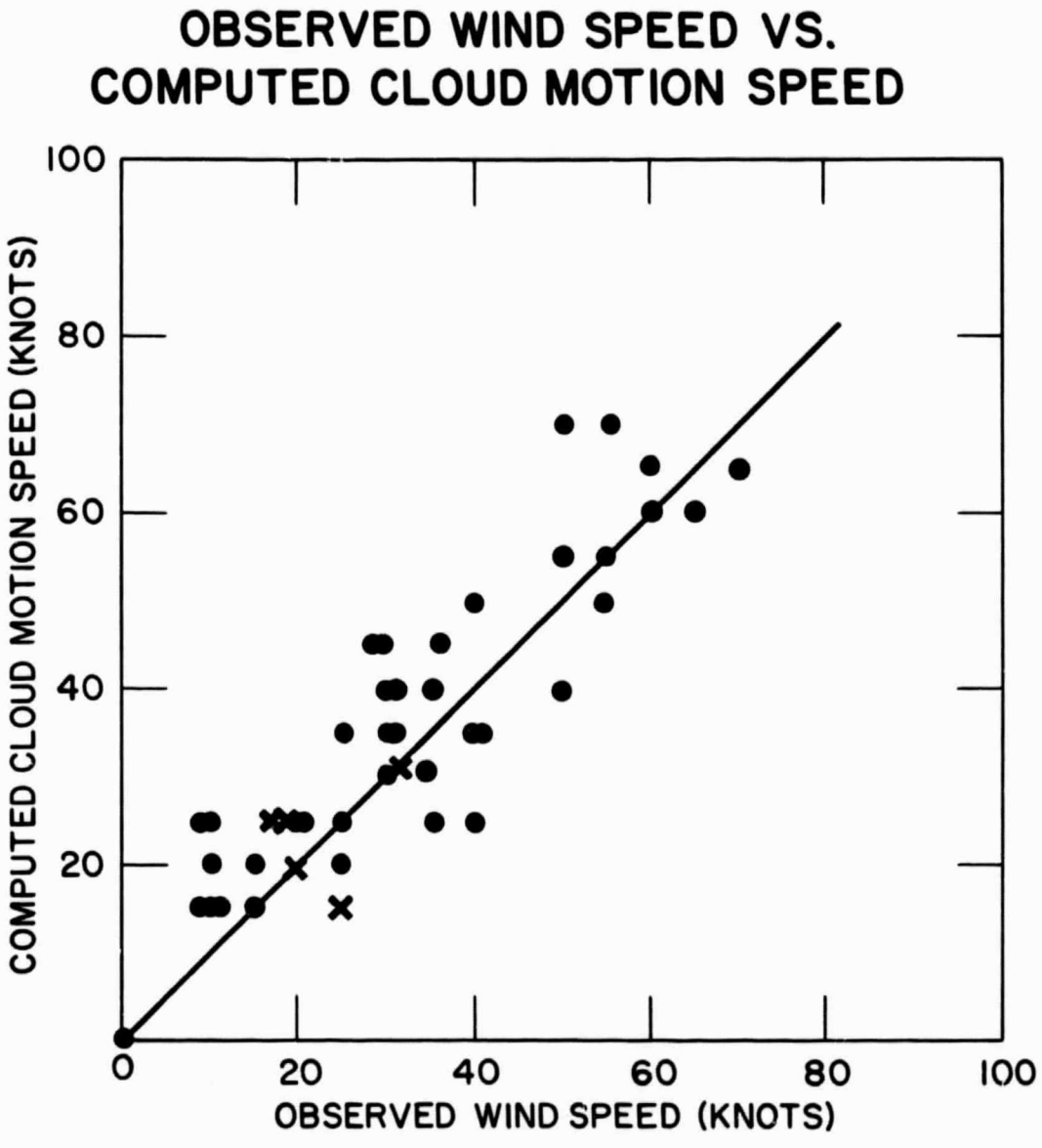

Figure 16. Scatter diagram of computed cloud motion speed versus observed wind speed.

TABLE 1

List of orbit pairs, midpoint time between orbits, and geographic features used to correct for relative attitude errors

Date	Midpoint Time (GMT)	Data Orbits	Geographic Features
September 15, 1966	0530	1636, 1637	Great Lakes
October 15, 1966	1425	2040, 2041	Kamchatka Pen.
October 28, 1966	0535	2208, 2209	Great Lakes
November 1, 1966	1545	2267, 2268	China Coast
November 8, 1966	1330	2360, 2361	China Coast
November 10, 1966	1410	2386, 2387	Kamchatka Pen.
November 11, 1966	1530	2400, 2401	Kamchatka Pen.

TABLE 2

Pertinent data on cloud position, computed cloud top pressure level, computed and observed wind vectors, and cloud size and effective cloud top temperature on each grid print map for the case of November 11, 1966

November 11, 1966 1530Z

Midpoint Cloud Position		Computed Cloud Top	Computed Cloud Motion		Observed Wind		First Map		Second Map	
Latitude	Longitude	Pressure Level (MB)	Direction (Degrees)	Speed (Knots)	Direction (Degrees)	Speed (Knots)	Cloud Size (Nautical Miles)	Effective T_{BB} (^{o}K) of Cloud Top	Cloud Size (Nautical Miles)	Effective T_{BB} (^{o}K) of Cloud Top
48.5^{o}N	146.5^{o}E	850	300	25	305	25	25 X 15	265	25 X 20	261
45.5^{o}N	144.0^{o}E	700	310	25	295	35	35 X 20	265	60 X 40	245
42.0^{o}N	138.0^{o}E	750	290	40	290	30	30 X 20	263	20 X 15	264
41.5^{o}N	136.0^{o}E	750	295	40	290	35	65 X 30	263	65 X 30	263
39.5^{o}N	135.5^{o}E	450	275	65	280	70	65 (cloud edge)	240	80 (cloud edge)	250
37.5^{o}N	131.5^{o}E	425	285	60	270	60	25 X 10	240	70 X 35	250
33.0^{o}N	132.5^{o}E	600	255	40	275	30	50 X 50	266	50 X 20	268

TABLE 3

Pertinent data on cloud position, computed cloud top pressure level, computed and observed wind vectors, and cloud size and effective cloud top temperature on each grid print map for the remaining six cases

Midpoint Cloud Position		Computed Cloud Top	Computed Cloud Motion		Observed Wind		First Map		Second Map	
Latitude	Longitude	Pressure Level (MB)	Direction (Degrees)	Speed (Knots)	Direction (Degrees)	Speed (Knots)	Cloud Size (Nautical Miles)	Effective T_{BB} (°K) of Cloud Top	Cloud Size (Nautical Miles)	Effective T_{BB} (°K) of Cloud Top
					September 15, 1966 0529Z					
*46.0°N	88.0°W	850	040	/ 20	010	/ 20	90 X 45	272	90 X 25	274
37.0°N	88.0°W	375	310	/ 30	300	/ 35	15 X 30	245	25 X 45	243
					October 15, 1966 1425Z					
42.5°N	151.5°E	700	160	/ 15	140	/ 10	60 X 25	268	50 X 50	268
42.5°N	156.0°E	525	240	/ 25	255	/ 20	30 X 20	263	25 X 40	260
					October 28, 1966 0534Z					
*54.0°N	62.0°W	875	260	/ 30	275	/ 30	50 X 50	262	35 X 35	262
*53.0°N	63.0°W	900	230	/ 15	270	/ 25	45 X 25	263	25 X 25	263
*53.5°N	65.0°W	900	245	/ 25	280	/ 20	35 X 15	260	25 X 35	263
54.0°N	67.0°W	725	280	/ 45	290	/ 30	10 X 30	256	25 X 25	256
54.0°N	73.0°W	800	270	/ 45	300	/ 30	20 X 50	257	45 X 10	260
*53.5°N	75.5°W	850	250	/ 25	280	/ 20	15 X 40	258	30 X 75	263
52.5°N	78.0°W	750	275	/ 35	290	/ 30	30 X 65	257	10 X 35	264
53.5°N	79.0°W	775	285	/ 35	295	/ 25	45 X 75	257	40 X 40	263
49.5°N	79.0°W	675	275	/ 35	280	/ 40	60 X 25	262	30 X 30	266
47.0°N	79.0°W	450	265	/ 60	275	/ 65	70 X 30	243	20 X 80	256
47.0°N	76.0°W	500	255	/ 65	280	/ 60	60 X 40	247	30 X 55	263

TABLE 3 - (CONTINUED)

Midpoint Cloud Position		Computed Cloud Top	Computed Cloud Motion		Observed Wind		First Map		Second Map	
Latitude	Longitude	Pressure Level (MB)	Direction (Degrees)	Speed (Knots)	Direction (Degrees)	Speed (Knots)	Cloud Size (Nautical Miles)	Effective T_{BB}(°K) of Cloud Top	Cloud Size (Nautical Miles)	Effective T_{BB}(°K) of Cloud Top
					November 1, 1966 1545Z					
41.0°N	135.0°E	750	290	35	280	40	40 X 15	264	60 X 25	263
41.5°N	132.5°E	750	260	25	290	40	140 X 70	262	180 X 100	263
					November 8, 1966 1330Z					
59.5°N	169.0°E	850	295	15	290	10	60 X 15	258	80 X 40	263
59.5°N	172.0°E	850	310	15	310	10	45 X 20	263	60 X 15	268
58.5°N	175.0°E	850	300	20	300	10	30 X 25	266	30 X 30	268
57.5°N	173.0°E	850	Calm		Calm		30 X 10	264	10 X 10	268
55.5°N	168.5°E	775	020	20	360	15	80 X 25	263	90 X 30	263
55.0°N	166.5°E	825	005	25	340	10	40 X 20	263	40 X 20	264
52.0°N	164.0°E	900	335	25	350	10	45 X 20	258	65 X 35	265
49.0°N	162.0°E	500	225	35	240	30	40 X 20	245	50 X 50	245
					November 10, 1966 1410Z					
63.5°N	178.0°W	925	325	20	330	25	30 X 10	265	40 X 30	263
58.0°N	180°	575	290	45	275	35	20 X 10	248	15 X 10	244
59.0°N	167.5°E	850	090	15	070	15	65 X 45	263	35 X 25	263
55.0°N	171.5°E	575	280	30	265	30	50 X 15	250	60 X 15	247
52.5°N	169.0°E	850	250	50	260	40	55 X 55	264	80 X 80	264
50.0°N	162.0°E	750	260	40	250	50	40 X 40	264	10 X 10	260
50.0°N	163.5°E	750	255	55	250	50	40 X 15	263	20 X 10	260
49.5°N	164.0°E	750	250	70	250	50	10 X 10	265	35 X 15	259
48.5°N	161.5°E	700	230	70	250	55	45 X 20	258	60 X 20	257
49.0°N	158.5°E	575	230	55	245	55	55 X 20	253	30 X 15	247
43.0°N	158.0°E	500	250	50	260	55	40 X 40	245	70 X 20	243

* possibly influenced by land